

Flow field and emission characterization of a novel enclosed jet-in-hot-coflow canonical burner

van den Berg, Thimo; Sampat, Rishikesh; Gangoli Rao, Arvind

DOI

[10.1016/j.jaecs.2024.100298](https://doi.org/10.1016/j.jaecs.2024.100298)

Publication date

2024

Document Version

Final published version

Published in

Applications in Energy and Combustion Science

Citation (APA)

van den Berg, T., Sampat, R., & Gangoli Rao, A. (2024). Flow field and emission characterization of a novel enclosed jet-in-hot-coflow canonical burner. *Applications in Energy and Combustion Science*, 20, Article 100298. <https://doi.org/10.1016/j.jaecs.2024.100298>

Important note

To cite this publication, please use the final published version (if applicable). Please check the document version above.

Copyright

Other than for strictly personal use, it is not permitted to download, forward or distribute the text or part of it, without the consent of the author(s) and/or copyright holder(s), unless the work is under an open content license such as Creative Commons.

Takedown policy

Please contact us and provide details if you believe this document breaches copyrights. We will remove access to the work immediately and investigate your claim.



Flow field and emission characterization of a novel enclosed jet-in-hot-coflow canonical burner

Thimo van den Berg, Rishikesh Sampat, Arvind Gangoli Rao *

Delft University of Technology, Faculty of Aerospace Engineering – Sustainable Aircraft Propulsion, Kluyverweg 1, Delft, 2629 HS, South Holland, The Netherlands

ARTICLE INFO

Keywords:

Flameless combustion
Mild combustion
Low NO_x
NO_x reburning
Jet-in-hot-coflow
Emissions
NO_x

ABSTRACT

The jet-in-hot-coflow is a canonical combustion setup, which has been used in several studies to study Flameless/MILD combustion and auto-ignition of fuels. However, the NO_x and CO emission measurements from these combustion setups were not possible due to the entrainment of laboratory air and a lack of a well-defined physical system limit. These limitations have been overcome by a new enclosed jet-in-hot-coflow setup. The combustor was operated by injecting a mixture of CH₄-Air in the central jet, and the coflow comprised of hot products from CH₄-Air combustion in burners upstream. The coflow composition was further controlled by adding diluents such as N₂ and CO₂. Measurements were done using stereoscopic particle image velocimetry, suction probe gas analysis, thermocouples, and chemiluminescence imaging. Increasing central jet velocity and equivalence ratio led to lower NO_x and a reaction zone that enlarged and shifted downstream. The reduction in NO_x emission was attributed to the reburning mechanism. Adding CO₂ and N₂ as diluents in the coflow resulted in a longer combustion zone and reduced temperatures in the combustion chamber, leading to decreased NO_x production and increased reburning. These experiments provide relevant flowfield and emissions data for modelers and help characterize combustion regimes such as Flameless/MILD.

1. Introduction

NO_x emissions can negatively impact human health, plant and marine life and also have a direct or indirect impact on the climate. At low altitudes, it can cause an increase in atmospheric ozone, which has a net global warming effect and is toxic for direct inhalation [1]. Additionally, these gases have been linked to exacerbate or cause asthma, chronic obstructive pulmonary disease (COPD), and various cardiovascular diseases [2,3]. Reducing NO_x emissions from combustion devices is therefore crucial. Flameless combustion (FC) is an unconventional combustion regime that produces low NO_x at high combustion efficiency [4]. It typically occurs when the reactants are at a high temperature (above the self-ignition temperature) and diluted such that there is a low O₂ concentration [5]. This results in a distributed combustion zone with reduced temperature peaks. As one of the main NO_x production mechanisms, the Zeldovich mechanism is strongly dependent on the temperature; a reduction in temperature peak will lead to a reduction in NO_x emissions [6].

One of the potential applications of FC is in sequential combustion systems, which are already employed in some gas turbines [7]. A hybrid engine concept employing a sequential combustor was proposed for use in a blended wing body aircraft as well [8]. In such a system, flue gases from a primary combustor are fed into a secondary combustor, resulting

in lower NO_x emissions due to the lower O₂ concentration and NO_x reburning occurring in the secondary combustor [7,9]. Attaining the conditions required for FC might also be easier in such a sequential combustor as the recirculation rate needed to obtain sufficiently high dilution levels is lower [4].

In the literature, terms such as MILD combustion, flameless oxidation (FLOX), and colorless distributed combustion (CDC) are used to describe a regime with similar properties but slightly differing operating conditions [4]. Several authors have defined formal definitions of this regime with varying degrees of overlap. The earliest definition is based solely on the recirculation of reactants, where if the ratio of recirculated mass flow of exhaust gasses over the fresh reactants is greater than 2, combined with a sufficiently high furnace temperature, this would result in attainment of the FLOX regime [10]. The perfectly stirred reactor definition (by Cavaliere and De Joannon [11]) defines MILD combustion as a regime where the temperature of the reactants is above their self-ignition temperature and the maximum temperature rise is below the self-ignition temperature ($\Delta T_{max} < T_{self-ign}$). Oberlack et al. [12] and Evans et al. [13] define the flameless regime based on the ignition behavior of premixed and non-premixed flames, respectively. The authors consider combustion to be flameless or MILD when there are no distinct ignition and extinction points but rather

* Corresponding author.

E-mail address: A.GangoliRao@tudelft.nl (A. Gangoli Rao).

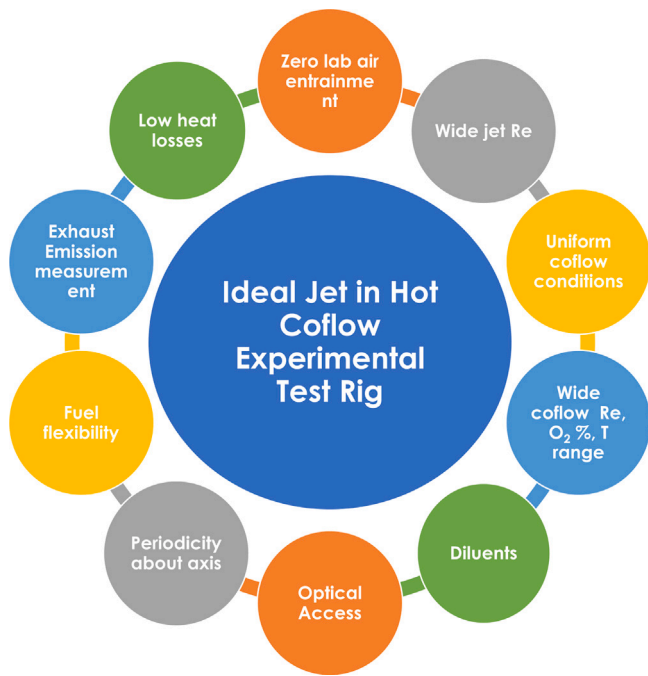


Fig. 1. Requirements of an ideal jet in hot coflow setup.

a smooth transition from an unburned to a burned state for flameless combustion. Evans et al. [13] provide a regime diagram showcasing the overlap and trends between the PSR and flamelet-based definitions as a function of inlet temperature and temperature change in the reaction zone. Though these definitions differ, they all describe a regime where the initial reactant temperature is high, the O_2 concentration is low, and the temperature change observed in the reaction zone is relatively small.

The jet-in-hot-coflow (JHC) configuration has been used to investigate FC over a wide range of operating conditions, allowing for easy adaptations of the diluent composition and temperature. A JHC burner is a sequential burner system where hot flue gases are produced by coflow burners in the coflow duct, which then interacts with the gas mixture emanating from the central jet. Most JHC setups reported in the literature, like the Adelaide burner [14] and the Delft-JHC burner [15], are open flames, allowing for ambient air entrainment, thereby influencing the ensuing reaction pathways and the measured gas composition. Further, slow-evolving emissions such as NO_x are sensitive to residence time and, therefore, to the location. Based on the observations from the literature and some critical thinking, we propose some requirements to define a good jet-in-hot-coflow setup, which are enlisted in Fig. 1

To address the limitations of existing JHC setups in preventing laboratory air entrainment and lack of system-level emissions measurements, we have developed an enclosed jet-in-hot-coflow setup such that the emissions from the combustor can be characterized. The central jet in this setup injects premixed fuel+air to emulate better the combustion in premixed Flameless combustors such as that used by Sadanandan et al. [16].

The flow field inside this new combustor is characterized using stereo particle image velocimetry (SPIV) under non-reacting conditions. Chemiluminescence, thermocouple, and gas analyzer measurements are employed during reacting flow experiments for various jet velocities, equivalence ratios, and O_2 concentrations. Additionally, the effect of diluents is investigated by adding CO_2 or N_2 to the coflow. Since FC is achieved by reducing the O_2 concentration in the reactants, it is interesting to look at the effect of dilution with CO_2 and N_2 . CO_2 can decompose into CO at high temperatures, which then starts competing

for hydrogen radicals, thereby depleting the radical pool quicker under vitiated conditions [17,18]. On the other hand, CO_2 has also been found to promote branching reactions at lower temperatures due to its higher third-body collision efficiency compared to N_2 [19].

2. Experimental setup

2.1. The combustor setup

The enclosed jet-in-hot-coflow setup, as shown in Fig. 2, is a vertical combustor setup consisting of a hot coflow of flue gases generated by two upstream secondary burners and a central jet, which produces the main combustion zone. For the current setup, a mixture of CH_4 -Air is fed through the central jet, which has an inner diameter of 3 mm. The hot flue gases in the coflow are produced by two burners at the bottom of the setup, each of which can provide about 6 kW in thermal power. They operate on a CH_4 -Air mixture, controlled independently from the central jet. Additional CO_2 and N_2 can be added to the coflow mixture through two diluent attachments at the bottom of the setup. The flue gases and inert diluents mix in the coflow duct and then emerge in the combustion chamber, which has an octagonal cross-section. This chamber has an inner diameter of 120 mm and is equipped with eight quartz glass windows, each with a width of 40 mm and a height of 300 mm. This allows for the streamwise observation up to 100 jet diameters. One of the quartz windows is replaced by a stainless steel plate with equally spaced ports, which allows for the insertion of a thermocouple or suction gas analyzer probe; an additional gas probe attachment is located close to the exhaust of the combustor. Cooling air is mixed into the exhaust of the combustor to cool the gases down to prevent damaging the exhaust duct. The exhaust probe extends into the gas to ensure it extracts gas before the cooling air is mixed in. The setup operates at atmospheric pressure, however, a conical section is used to create a small pressure drop of about 80 mbar between the combustion chamber and the exhaust to prevent back flow of cooling air into the reaction zone. The coflow duct and bottom flange of the combustion chamber are insulated by layers of alkaline earth silicate (AES) blankets to minimize heat losses as shown in Fig. 2.

The flow of reactants and diluents to the coflow burners, central jet, coflow, and cooling system is controlled by Bronkhorst EL-flow mass flow controllers, which have an accuracy of $\pm 0.5\%$ of reading and $\pm 0.1\%$ of full scale. The O_2 % in the coflow is controlled by altering the equivalence ratio and power of the coflow burners, and by changing the flow rate of the additional diluent.

2.2. Measurements & diagnostics

The flow field inside the combustor was characterized by stereo particle image velocimetry (SPIV) under non-reacting conditions. DEHS oil seeding particles were generated using a PIVTEX aerosol generator, producing droplets of approximately 1 μm diameter through Laskin nozzles. These tracer particles were added to the coflow while the central jet was unseeded but entrained particles from the coflow. A Quantel Evergreen double pulse Nd:YAG laser with pulse energy set to 120 mJ at 532 nm was used to produce a laser sheet of 150 x 45 x 1 mm (length x height x thickness) in the region of interest. Two Imperx Bobcat IGV-B1610 CCD cameras (1628 x 1236 pixels, with a pixel size of 4.4 μm) were used to capture the flow. Each camera was equipped with a 105 mm AF Nikkor lens, with a selected f-stop of 11. With this f-stop, the imaged particle size is about 2 pixels on the sensor. A 532 nm bandpass filter was placed over each lens to filter out background noise. Additionally, the lens was connected to the camera using a Scheimpflug adapter. The synchronization between the camera and the laser was done using a LaVision programmable timing unit. For each case, 800 images were taken, which were processed in DaVis 8.4.0. Processing was done in multi-pass mode with decreasing window size and a final pass window size of 24 x 24 pixels with 75% overlap. Finally, error

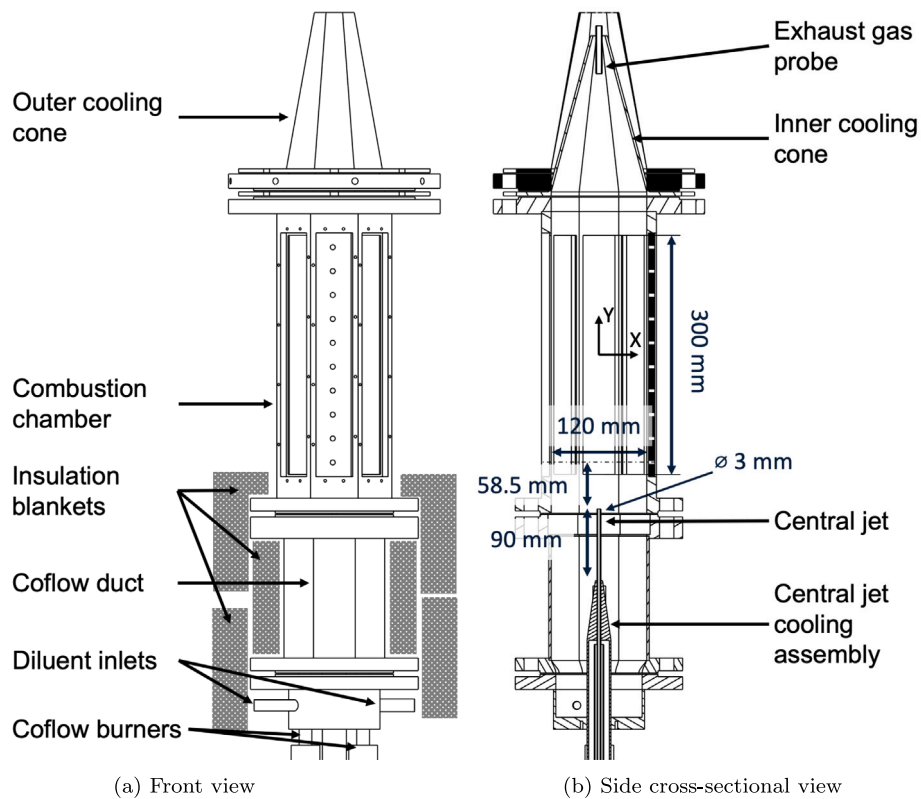


Fig. 2. Diagram of the enclosed jet-in-hot-coflow combustor.

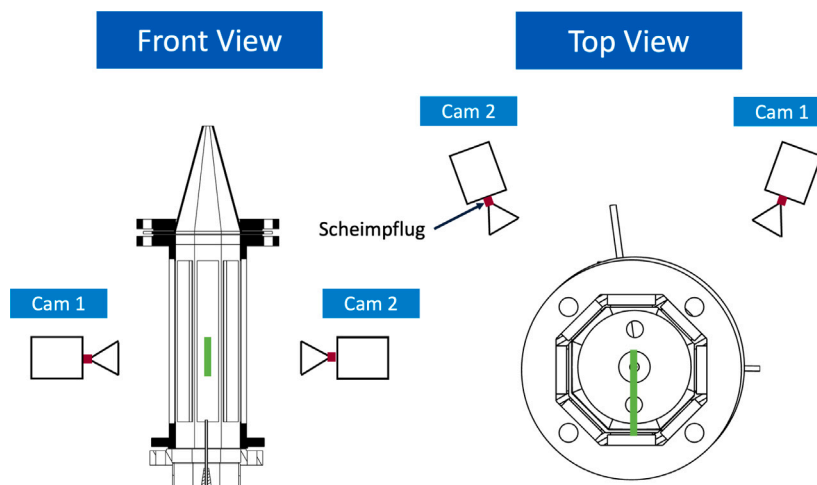


Fig. 3. Diagram of the location of the SPIV cameras relative to the combustor. The green line indicates the approximate location of the field of view.

margins are provided for a 95% confidence interval using the large sample theory described by Benedict and Gould [20].

The cameras were placed on either side of the setup, each looking at a different side of the laser sheet. Due to the frame of the combustion chamber, each camera could only see slightly more than half the width of the chamber. The field of view starts from about 58 mm to 92 mm from the jet exit. In Fig. 3, a schematic of the camera location, the laser sheet, and the field of view are shown relative to the combustor setup.

Gas analysis was done using an ABB gas analyzer consisting of three modules. CO, CO₂, and CH₄ were measured by the Uras26 module (utilizing IR-absorption), O₂ by the Magnos28 paramagnetic analyzer module, and NO by the Limas21 module, using Differential UV Resonance Absorption Spectroscopy (DUV-RAS). The gas was sampled using a suction probe with a 6 mm outer diameter and 3 mm inner diameter.

All species were measured on a dry basis, i.e. the water was condensed out, except for NO, which was done 'hot-wet'. The sampling line is maintained at a temperature of 180 °C and the Limas module at 80 °C. Although NO has a low solubility in water, there may be a systematic error due to water condensation. However, as most of the gas volume (> 90%) comes from the coflow, which is kept constant across all operating conditions, the deviation will be similar across cases. Thus, the trends are valid. It should be noted that the hot-wet NO measurement method used has a lower loss of NO due to dissolution compared to the dry measurement method, as is typically used in literature. Temperature measurements inside the combustion chamber were performed using an S-type thermocouple with a platinum (10%) sheath, having an external diameter of 3 mm.

Table 1

Streamwise distance from the jet exit to all measurement ports.

Port number	1	3	5	7	10	Exhaust
Downstream location [Y/D_{jet}]	19.5	39.5	59.5	79.5	110	182

Table 2

Flow conditions in the central jet and coflow in the reacting experiment. The jet has a reference temperature of 300 °C, and the coflow a reference temperature of 1000 °C.

	Flow rate [lnpm]	Velocity [m/s]	Reynolds [-]
Low-velocity jet	22.2	110	$6.87 \cdot 10^3$
Baseline jet	33.3	165	$10.3 \cdot 10^3$
High-velocity jet	44.4	220	$13.8 \cdot 10^3$
Coflow	203	1.32	$1.76 \cdot 10^3$

Table 3

Coflow settings for different added diluent flow rates in the reacting experiment.

	Power [kW]	ϕ_{pb} [-]	O ₂ [%]	Dry O ₂ [%]
No diluent	11.1	0.958	0.81	0.98
20lnpm	9.92	0.953	0.81	0.97

Table 4

Composition of the coflow for different added diluent flow rates in the reacting experiment.

Gas	Flow rate [lnpm]	O ₂ [%]	H ₂ O [%]	CO ₂ [%]	N ₂ [%]
No added diluent	N/A	0.81	18.3	9.1	71.8
N ₂	20	0.81	16.4	8.2	74.6
CO ₂	20	0.81	16.4	18.0	64.7

The streamwise centerline measurements were taken by inserting the probe into different ports of the measurement plate, which replaced one of the windows of the combustion chamber. This plate has ten ports, equally spaced 30 mm apart. Ports 1, 3, 5, 7, and 10 were used for gas composition analysis and temperature measurements. The exhaust gas composition was also measured using a probe inserted into the cooling cone, as shown in Fig. 2. The distances from the jet exit to these measurement ports are provided in Table 1, where the jet exit is at $Y = 0$.

Radial measurements of the combustion chamber were done at Port 1, located at $Y/D_{jet} = 19.5$ from the jet exit, using a Zaber traverse system by moving the probe with a uniform velocity from the center to the wall of the chamber. The probe moved at 0.62 mm/s for the temperature measurements, and for the gas analyzer, the probe velocity was 0.42 mm/s. For both measurements, data collection was performed at 10 Hz. As the insertion of a probe perturbs the flow, the measured values were averaged over a characteristic length, chosen to be the outer diameter of the probe. This resulted in an average of 71 data points per measurement location for the thermocouple measurement and 97 data points for the gas probe. The 95% statistical confidence interval is then calculated based on the sliding average.

The thermocouple measurements were corrected using Eq. (1) [21].

$$\frac{Nu \cdot k_g}{d} (T_g - T_{th}) = \epsilon \sigma (T_{th}^4 - T_w^4) \quad (1)$$

Nu is the Nusselt number for the thermocouple, which was evaluated using Eq. (2), k_g the thermal conductivity of the gas, d the diameter of the thermocouple, T_g the gas temperature, T_{th} the temperature measured by the thermocouple, ϵ the emissivity of the thermocouple and σ the Stefan-Boltzmann constant.

$$Nu_{cyl} = 0.3 + \frac{0.62 \cdot Re^{1/2} \cdot Pr^{1/3}}{(1 + (0.4/Pr)^{2/3})^{1/4}} \left(1 + \left(\frac{Re}{282000} \right)^{5/8} \right)^{4/5} \quad (2)$$

The value for the emissivity of the thermocouple was found using Eq. (3) [22], where T is the thermocouple temperature.

$$\epsilon_{S-type} = -0.1 + 3.24 \cdot 10^{-4}T - 1.25 \cdot 10^{-7}T^2 + 2.18 \cdot 10^{-11}T^3 \quad (3)$$

Chemiluminescence imaging of the combustion zone was done using a Nikon D7500 DSLR camera. As the signal was faint, the images were obtained over long exposure times of the order of 2 ms. Thus, each image already consisted of an implicit average of the fluctuating flame. To reduce noise from the glowing chamber, the instantaneous images were background subtracted, where the background was obtained by taking the average over all images. The resultant images were used to produce average images referred to as “flame image”.

2.3. Reacting conditions

A baseline jet of 165 m/s, a high-velocity jet of 220 m/s, and a low-velocity jet of 110 m/s, evaluated at 300 °C, were chosen as the operating conditions, as shown in Table 2. The equivalence ratio of the central jet was varied between 0.6 and 1.5 while keeping the jet velocity constant to maintain a constant residence time in the combustion chamber. Due to the changing equivalence ratio, the power of the main burner was also varied; the plot in Fig. 4(a) shows the power of the main burner as a function of the equivalence ratio of the central jet for the three jet velocities. The global O₂ % is the molar fraction of O₂ if the coflow gases and the central jet gases were perfectly mixed before ignition. This is shown in Fig. 4(b) for the three jet velocities as a function of the central jet equivalence ratio. The coflow conditions were kept constant between all of these cases, resulting in a slight change in the O₂% when the equivalence ratio of the central jet changes; about 1% of dry O₂ is left in the coflow gases.

The volume flow rate in the coflow was kept constant when adding diluents by reducing the power of the coflow burners, and the O₂% was kept constant by altering the equivalence ratio of the coflow burners. The configuration of the coflow burners are tabulated in Table 3. The composition of the coflow under the influence of the added diluents is given in Table 4

3. Results

3.1. Flow field characterization

An overview of the flow rates, bulk velocities, and Reynolds numbers is provided in Table 5. For the central jet, two jet velocities were used: a low-velocity case (97 m/s) and a high-velocity case (119 m/s). These conditions are different from those of the reacting condition measurements. However, they are similar enough to represent the flow physics qualitatively. A Reynolds number greater than 10,000 was chosen in the central jet to ensure the jet was fully turbulent. The large velocity difference between the central jet and coflow presents a problem; a tracer particle displacement of 10 pixels is desired, and a minimum of 0.1 pixels is detectable, but these conditions cannot be met for both the coflow and jet region using a single laser pulse separation time (dt). Therefore, three timings were used: 1.5 μ s when imaging the jet region, 100 μ s when imaging the coflow region, and 750 μ s when imaging the flow when the central jet was turned off.

In Fig. 5, the vertical velocity V_y is plotted in the coflow region for three operating conditions. The Y -axis shows the downstream distance from the jet exit, while the X -axis shows the radial location. The central jet is located at $Y = 0$, and this particular figure represents measurements at an axial distance between 20–30 jet diameters downstream of the central jet exit. As explained earlier, varying inter-frame time differences had to be used to capture the fast-moving jet and the slow coflow due to the limited dynamic range of PIV. Thus, in this figure, only the coflow is captured, and the jet region is not shown. A region of

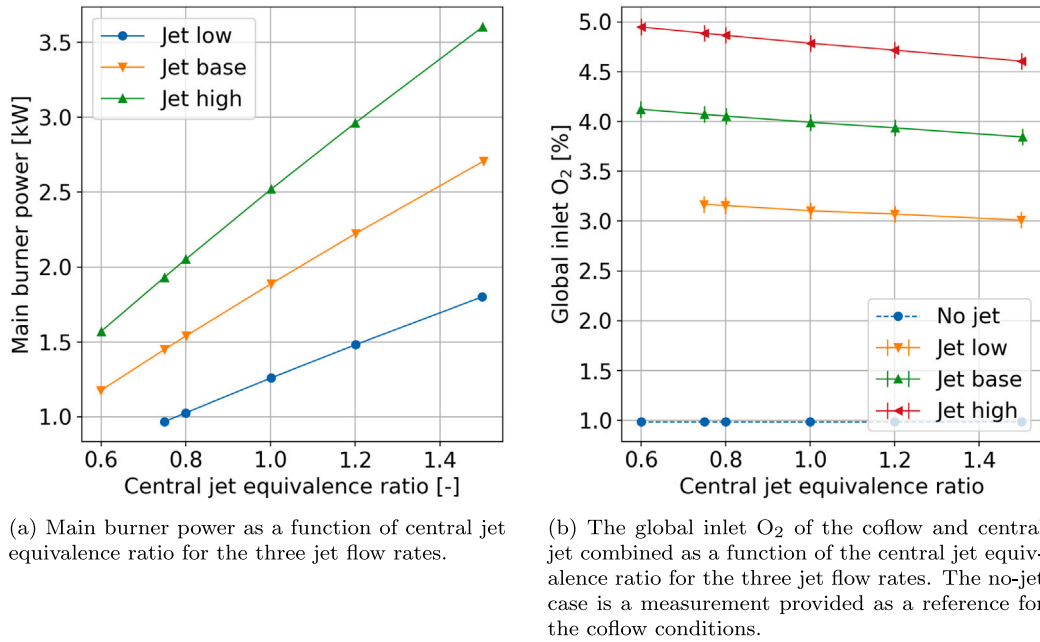


Fig. 4. Reacting flow operating conditions.

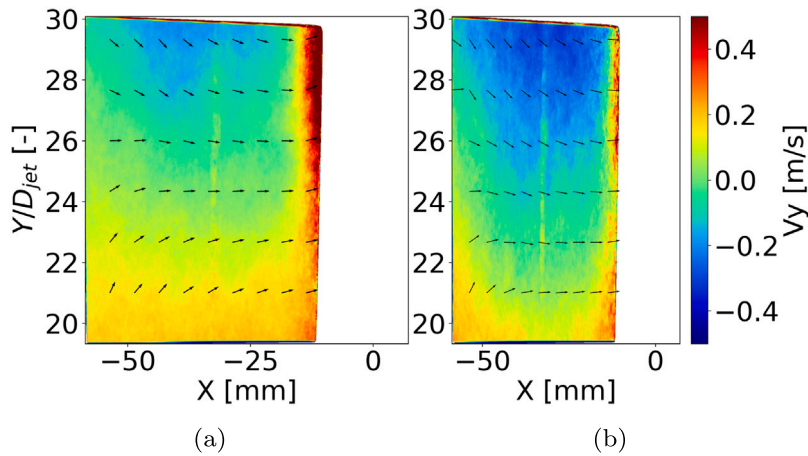


Fig. 5. The axial velocity inside the combustion chamber in the coflow region for three operating conditions: (a) Baseline jet (b) High-velocity jet. Jet centerline is located at $X = 0$ mm.

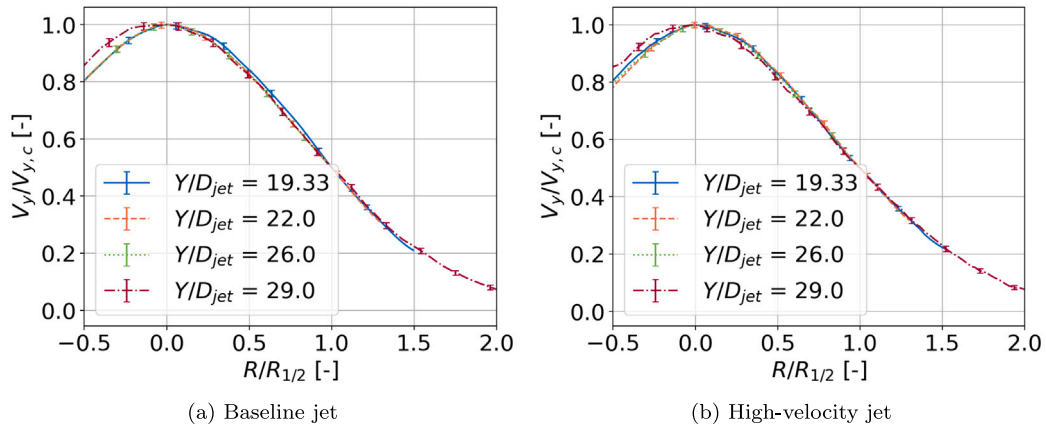


Fig. 6. Axial velocity V_y as a function of radial location R at four streamwise locations, for the (a) baseline jet and (b) high-velocity jet case.

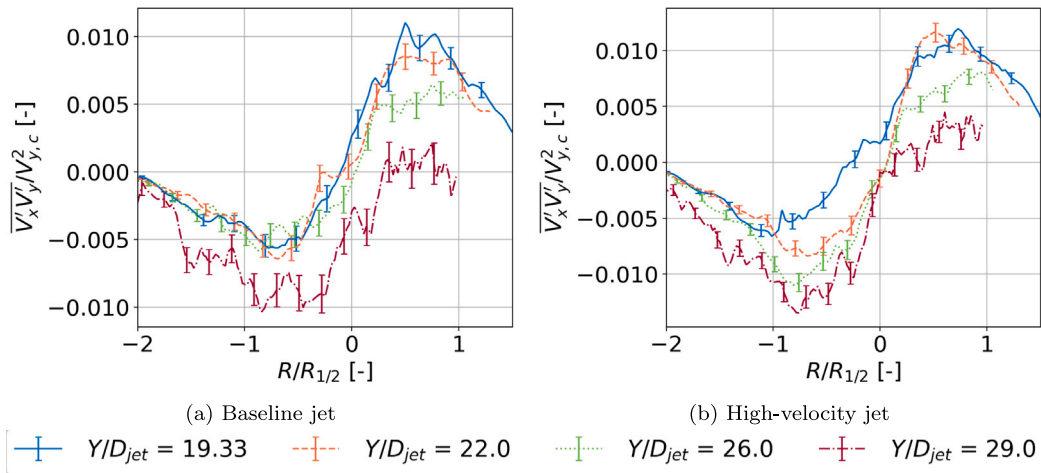


Fig. 7. Reynolds stress as a function of radial location R at four streamwise locations, for the (a) baseline jet and (b) high-velocity jet case.

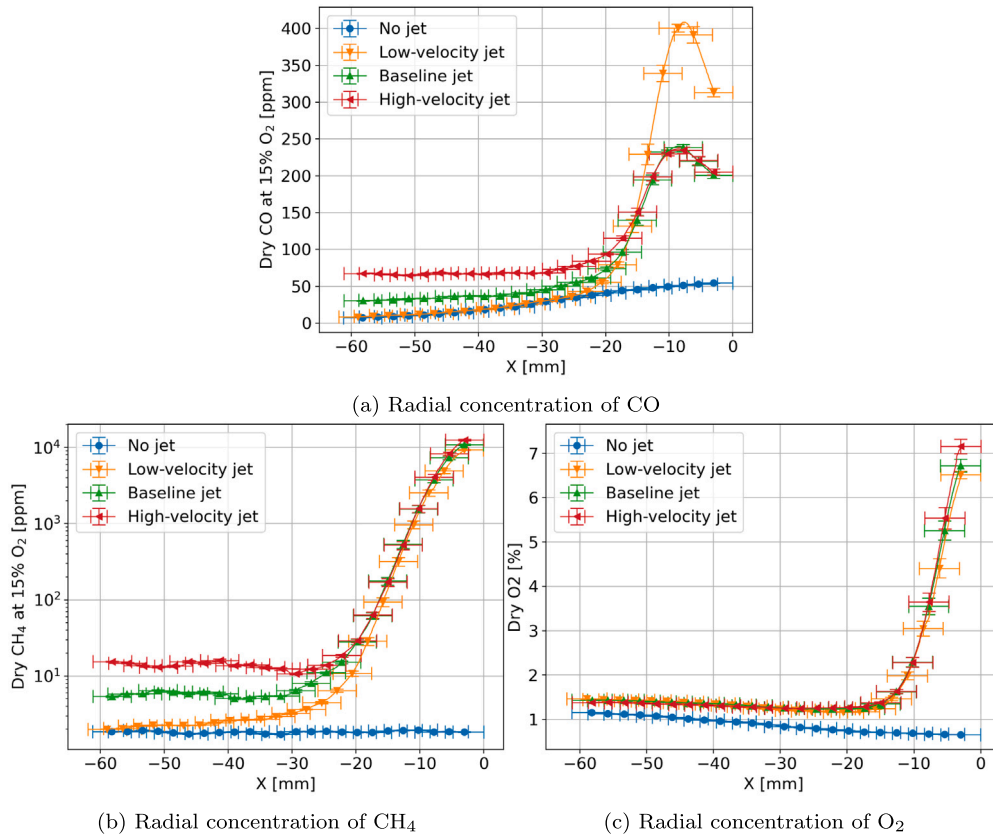


Fig. 8. Gas concentrations for various jet velocities with $\phi_{c_j} = 1.0$, measured at Port 1 ($Y/D_{jet} = 19.5$ from the jet exit).

Table 5

Overview of operating cases in the non-reacting experiment. Bulk velocities and Reynolds numbers are calculated at 20 °C.

Case	Central jet			Coflow		
	Flow rate [lnpm]	V_{bulk} [m/s]	Re [-]	Flow rate [lnpm]	V_{bulk} [m/s]	Re [-]
Baseline jet	38.4	97.1	$19.4 \cdot 10^3$	232	0.35	$2.6 \cdot 10^3$
High-velocity jet	47.1	119	$23.7 \cdot 10^3$	232	0.35	$2.9 \cdot 10^3$

negative V_y is observed in all three cases, indicating that a recirculation zone is present.

The Craya–Curtet number is a criterion that can be used to estimate if a recirculation zone will form and is given by

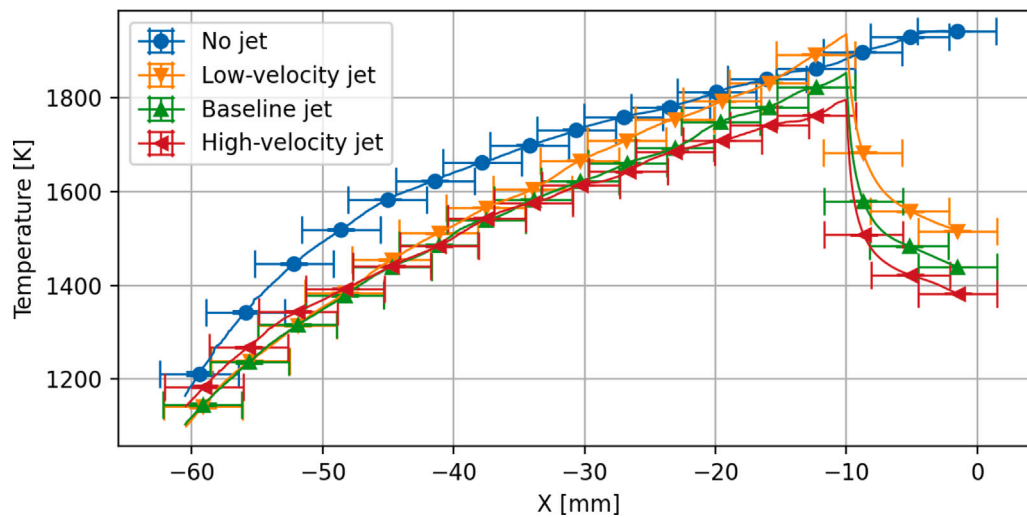


Fig. 9. Radial temperature profile for various jet velocities at $\phi_{c_j} = 1.0$, measured at Port 1 ($Y/D_{jet} = 19.5$).

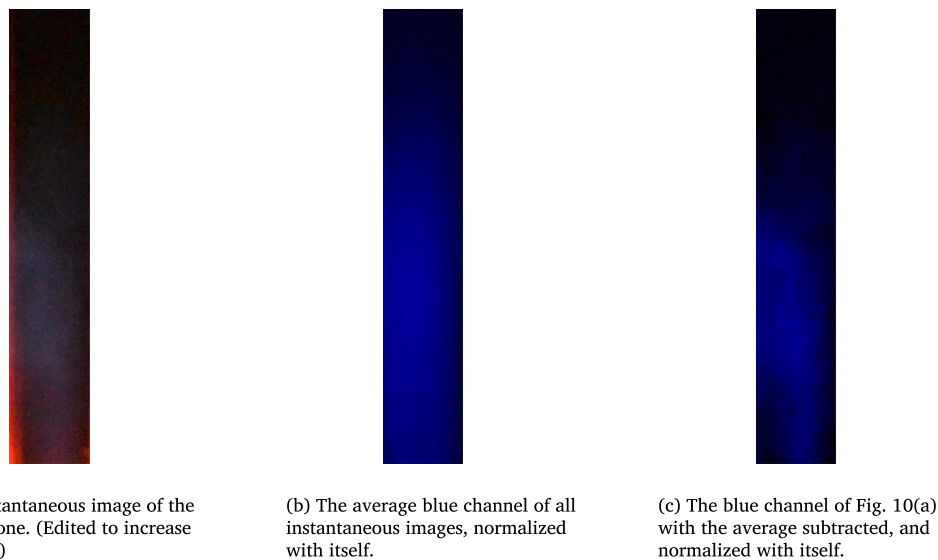


Fig. 10. The processing steps for obtaining the flame image for baseline jet velocity case, with $\phi = 0.75$.

$$C_t = \frac{(V-1)D^2 + 1}{D(V^2 - V - 0.5D^2(V-1)^2)^{0.5}}, \quad (4)$$

where V is the ratio of jet velocity to the coflow bulk velocity, and D is the ratio of the jet diameter to the coflow diameter. If $C_t > 0.75$, the jet can be assumed to be free, and a recirculation zone will not occur [23]. In Table 6, the Craya-Curtet number is tabulated for the three cases shown in Fig. 5, and the values being < 0.75 confirm that recirculation zone would form for these flow conditions.

The axial velocity profile of the jet is shown in Fig. 6(a) for the baseline jet case and in Fig. 6(b) for the high-velocity jet case. The velocity has been normalized by the peak velocity at that streamwise location $V_{y,c}$, and the radius has been normalized with the half-width of the jet. The Reynolds shear stress (RSS) is shown in Figs. 7(a) and 7(b) for the baseline jet and high-velocity jet cases. In the baseline jet case in Fig. 7(a), the lines for 19, 22, and 26 jet diameters away from the jet exit overlap for a large part, but the data at 29 jet diameters is shifted lower. The mean axial velocity profiles suggest that the jet may have achieved self-similarity; however, the RSS profiles show otherwise, and this may be due to the effect of confinement and the resultant recirculation zone being formed.

Table 6

Jet, coflow velocity and Craya-Curtet number for three operating conditions, with the jet and coflow at $P = 1$ atm, $T = 20$ °C.

		Baseline jet	High-velocity jet
Jet velocity	[m/s]	97	119
Coflow velocity	[m/s]	0.35	0.35
Craya-Curtet number	[-]	0.17	0.14

3.2. Coflow composition and temperature

In Figs. 8(a) 8(b), and 8(c) the dry CO, CH₄ and O₂ concentration as a function of radial location are displayed. The X -axis shows the distance from the centerline of the combustor in millimeters, with the wall of the combustion chamber being 62 mm from the centerline. All three jet velocities are displayed with a stoichiometric central jet. Additionally, the no-jet case is plotted, showing the gas composition in the coflow. The first observation that can be made is that the CO concentration peaks in the shear layer when the central jet is on, with the highest concentration in the low jet velocity case. Correlating this to the O₂ concentration in this area shows a concentration of approximately 4% for all three jet cases. On the centerline the O₂ concentration

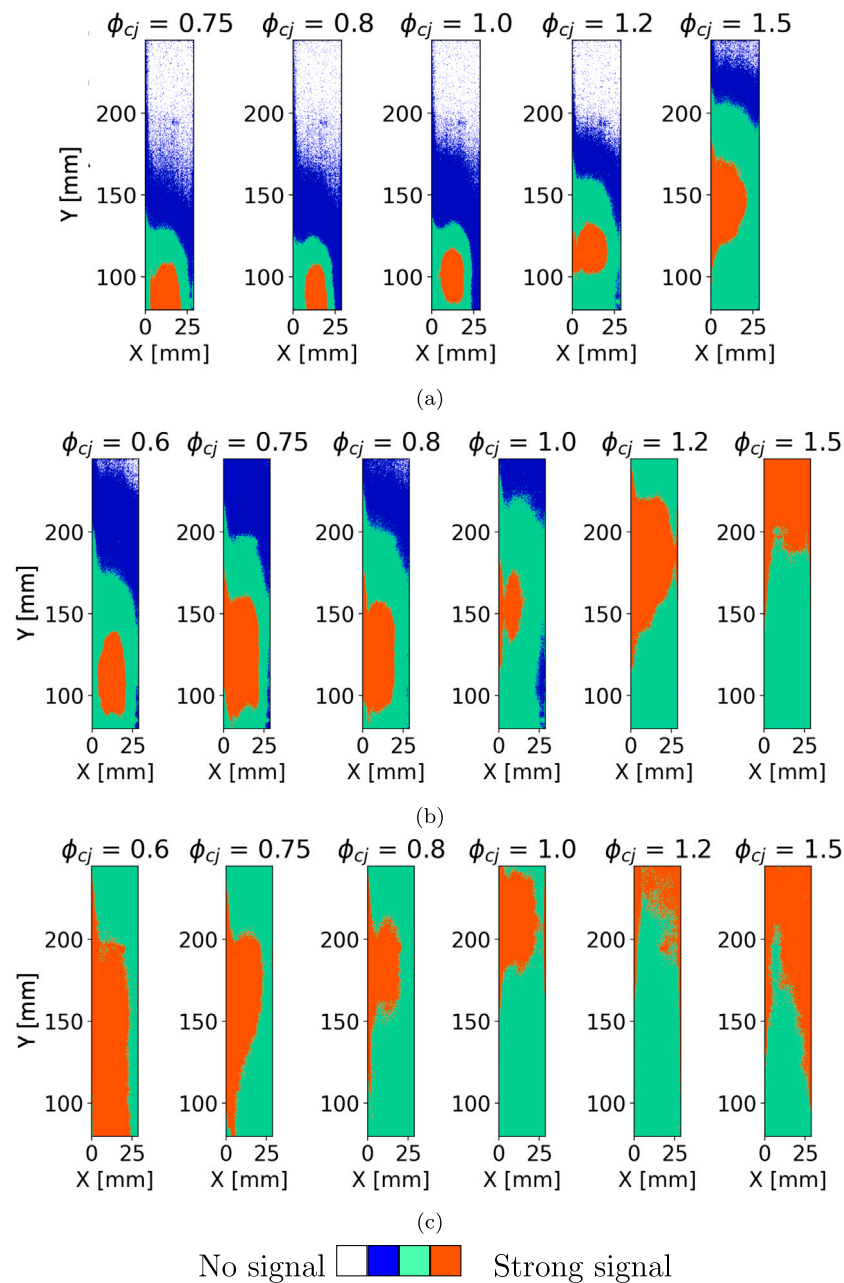


Fig. 11. Flame image of the reaction zone at different equivalence ratios for (a) low-velocity jet (b) baseline jet (c) high-velocity jet.

is about 7%, with the high velocity jet case having a slightly higher concentration, while the baseline and low velocity jet having slightly lower concentrations. This all indicates that the reactions are occurring under vitiated conditions. Furthermore, it can be seen that the CO and CH₄ concentrations in the coflow region are higher for the baseline and high jet velocity cases than the no-jet case. This can be explained by the recirculation zone observed in the cold-flow SPIV experiments. This recirculation zone transports gases from downstream back upstream in the coflow region, leading to the observed increase in CH₄. The fact that both CH₄ and CO are found in the recirculation zone indicates that combustion may still occur there, although the CH₄ concentration observed is relatively low.

The radial temperature for the same cases, measured at Port 1 ($Y/D_{jet} = 19.5$ from the jet exit), is shown in Fig. 9. The temperature in the coflow is lower in cases with jet than in the no-jet case, which could be attributed to the recirculation zone, which brings excess gas mass in this region, leading to a lowering of the temperature. The temperature

in the jet (-10 to 0 mm) is significantly lower than the gas temperature in the no-jet case at that location. In the coflow region (-60 to -10 mm), a significant radial temperature gradient can be seen, where a temperature drop of around 300K occurs over a distance of 30 mm. Thus, the mixture resulting from the entrainment of coflow gases in the jet could have a higher autoignition delay time.

3.3. Chemiluminescence

In Figs. 11(a), 11(b) and 11(c), the flame image plots of the reaction zone for the low-velocity jet, baseline jet, and high-velocity jet are shown for a range of equivalence ratios. These images are derived from a series of images taken over time. An example of an image is shown in Fig. 10(a). This image was obtained while running the central jet at the baseline jet velocity, with $\phi = 0.75$. Though it is hard to see in Fig. 10(a), the flame appears as a very faint, wispy blue form in the center of the frame. The image in Fig. 10(c) is the same image but with

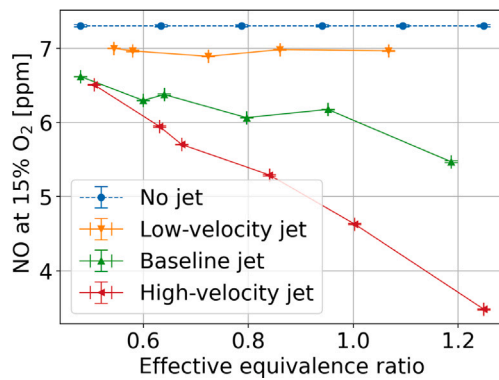


Fig. 12. Measured NO at the exhaust.

the average brightness over time subtracted from it, only the blue rgb channel shown and after being normalized with itself to enhance the brightness of the pixels. A self-normalized version of the average blue channel values is shown in Fig. 10(b). The presented flame image plots are obtained by summing the images as presented in Fig. 10(c) and then normalizing them with themselves.

For the low-velocity jet case, the flame visually appeared compact and fluctuated in a smaller area than the higher-velocity jet cases. This can also be seen from the comparatively smaller green and orange contour in Fig. 11(a), located at the bottom of the field of view. The area with the strongest signal moves downstream when the equivalence ratio increases; the size of the green and orange contour also grows with the increasing equivalence ratio. This same trend is observed with the baseline jet case. In the richest case ($\phi_{c,j} = 1.5$) with the baseline jet velocity, it even seems that the area with the strongest signal has moved beyond the field of view of the camera. Furthermore, comparing the low and baseline velocity jet velocities, it can be seen that the reaction zone is broader and has moved downstream with the increase in jet velocity. In the high jet velocity cases, with $\phi = 1.2$ and 1.5 , the region with the strongest signal also seems to have moved beyond the field of the camera. The orange area that extends down the sides of the image in these rich cases is likely to be caused by the light produced by the glow of the hot frame of the combustion chamber.

3.4. Exhaust gas measurements

The gas composition was measured at the exhaust port for all cases. In Fig. 12, the NO concentration is displayed as a function of the effective ϕ , which is obtained when also considering the O_2 in the coflow. The NO concentration measured in the no-jet condition is also displayed as a reference. The first thing to note in this plot is that the NO concentration observed when the central jet is on is lower than when there is no jet. This can either be because the NO produced in the central jet is much lower than the NO produced in the coflow and results in a mixture with a lower concentration, or the NO produced in the coflow is dissociated in the combustion zone produced by the central jet.

The trend as a function of the equivalence ratio is also interesting. One would expect a peak in NO concentration around stoichiometry, but this is not observed here. For the low jet velocity, the effective equivalence ratio does not seem to influence the NO concentration at all, while for the baseline and high jet velocities, a downward trend in NO concentration is observed with increasing equivalence ratio.

The CH_4 and CO concentrations at the exhaust are plotted in Figs. 13(a) and 13(b) respectively. For the high-velocity jet, $\phi \geq 1$ cases, there is still a notable amount of CH_4 and CO at the exhaust, thus indicating that combustion is incomplete inside the combustion chamber. This might also explain the low NO concentration observed

for these conditions in Fig. 12. However, the CO and CH_4 levels are low for the rest of the cases, indicating the operating limit for achieving complete combustion in this setup.

3.5. Centerline measurements

The O_2 and CH_4 concentration measured on the centerline of the combustor are plotted as a function of downstream distance from the jet exit are presented in Fig. 14 for the stoichiometric cases only. In Figs. 15 and 16, the CO and NO concentration are presented for all equivalence ratios and jet velocities.

A high concentration of CH_4 is observed at port 1, at which point an oxygen concentration is around 7%–8%. The peak in centerline CO concentration is observed further downstream for these stoichiometric cases, where the oxygen concentration is even lower. Combining these results with the radial measurements presented in Fig. 8 clearly show that combustion takes place under vitiated conditions. The jet is able to entrain the vitiated coflow at a fast enough rate to ensure a low O_2 concentration during the combustion of CH_4 .

Then, looking at the effect of changing jet velocity on CO in Fig. 15, the low jet velocity shows a steep increase in CO, peaking at port 3 and then dropping quickly. The stoichiometric baseline jet case shows a gradual increase and a lower concentration peak, achieved at port 5. This trend also continues for the stoichiometric high-velocity jet case, for which the peak in CO is only reached at port 7 and for which CO is above zero, indicating that combustion has not yet been completed by this point. Thus, it can be concluded that the size of the combustion zone increases with the increasing jet velocity.

Now, looking at the effect of ϕ , a similar trend can be observed. It is important to reiterate that for the change in ϕ , the total volume flow rate in the central jet and, thus, the jet velocity is kept constant. The leanest baseline velocity jet case ($\phi_{c,j} = 0.6$) shows a steep increase in CO and peaks at port 3, just like the stoichiometric low-velocity jet case. However, unlike the stoichiometric low-velocity jet case, the CO value does not drop as rapidly. With this increase in ϕ , it can also be seen that CO remains higher after the peak has been reached, indicating that the length of the combustion zone is also increasing with ϕ . It can thus be concluded that an increase in equivalence ratio leads to both a downstream movement where the CO peak is reached and an overall increase in the length of the combustion zone. For the richest baseline jet case, the exhaust CO concentration is above 200 ppm indicating that in this case, the combustion cannot be completed inside the combustion chamber.

Looking at the streamwise NO mole fraction Fig. 16, it can be seen that the value for nitric oxide is always lower when the central jet is turned on as compared to the no-jet case. Additionally, a trough can be seen for each plotted case when the jet is on. This indicates that there are regions in the combustion zone where NO consumption dominates production, while there are other regions in which production dominates. For the rich baseline jet cases and the stoichiometric high-velocity jet case, an initial rise in NO can be seen close to the jet exit, which is not present for the lean baseline jet cases and the stoichiometric low jet velocity case.

If the peaks of CO in Fig. 15 are compared with the troughs of NO in Fig. 16, a correlation can be found. Shortly after a peak in CO is reached, a trough in NO is reached. This indicates that while the CO concentration is high, and thus likely also the concentration of other carbon radicals, NO reburning is dominant over NO production, and therefore also that when the length of the combustion zone grows, the region in which NO reburning is dominant also grows.

In Fig. 17, the centerline temperature is plotted as a function of the distance from the jet exit. The low-velocity jet case has a clear peak at port 3. However, the baseline jet and high-velocity jet cases have a nearly uniform temperature distribution along the length of the chamber. The no-jet case has a much higher temperature at Port 1 than the jet cases and then has a monotonic decrease, with the temperature at Port 10 being lower than the other cases. The temperature difference of 700 K in this case is an indication of the extent of heat loss that occurs in this chamber.

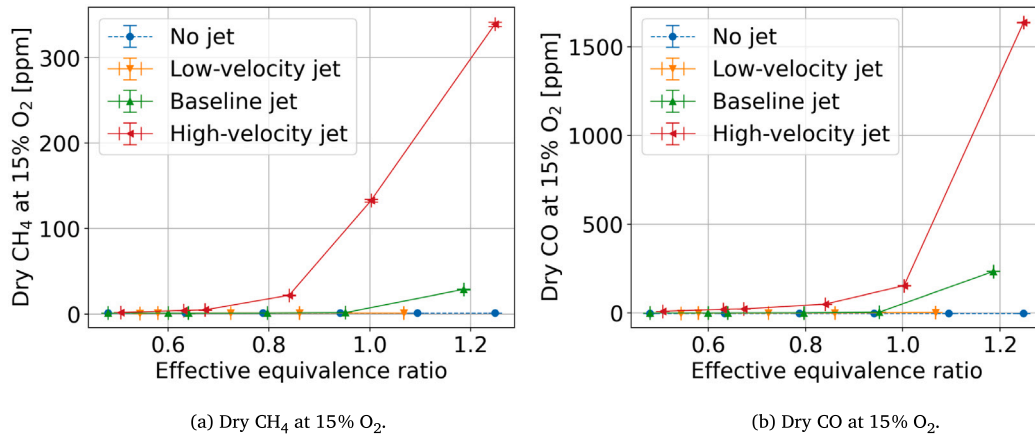


Fig. 13. Exhaust gas measurements at various jet velocities

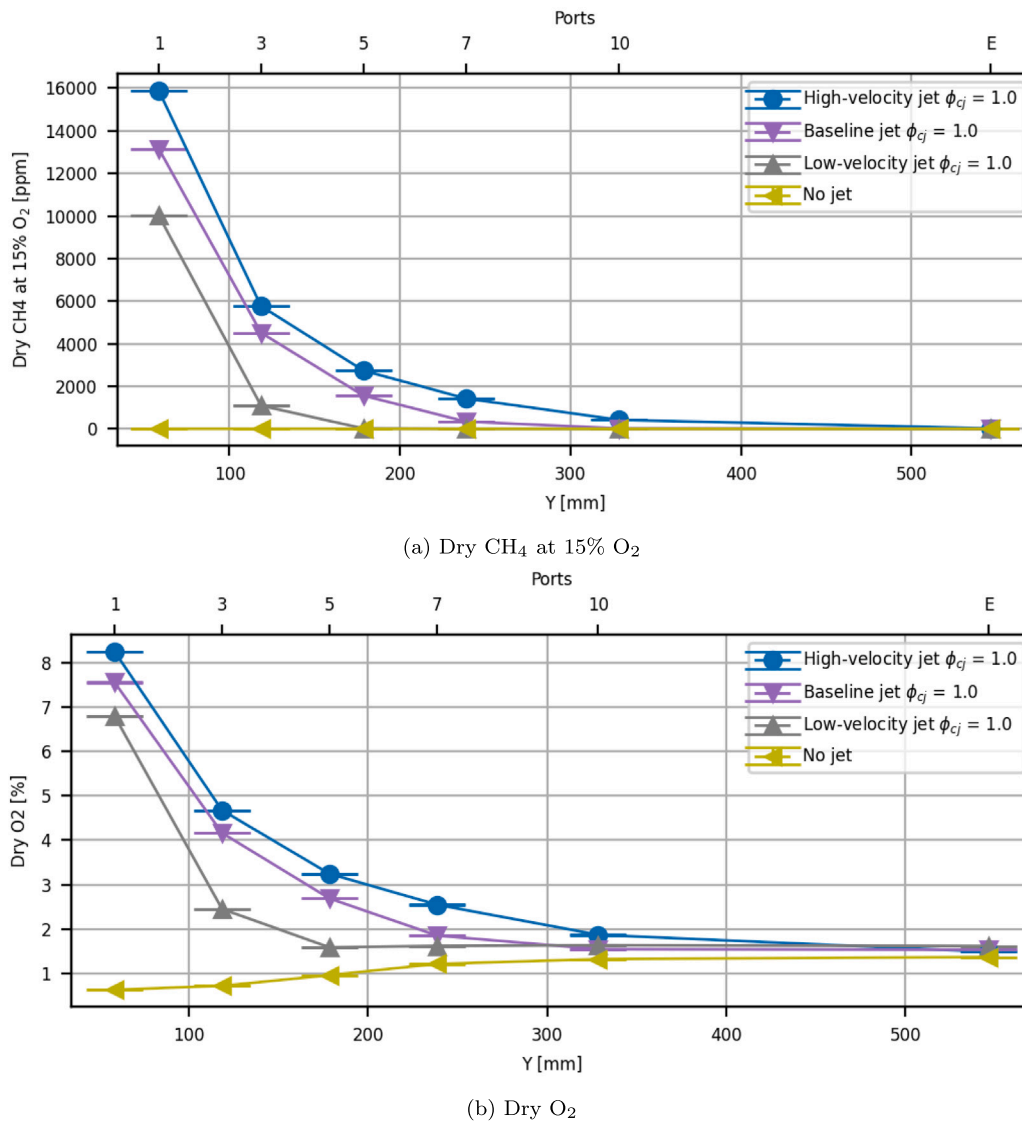


Fig. 14. Streamwise centerline measurements of various jet velocities under stoichiometric conditions.

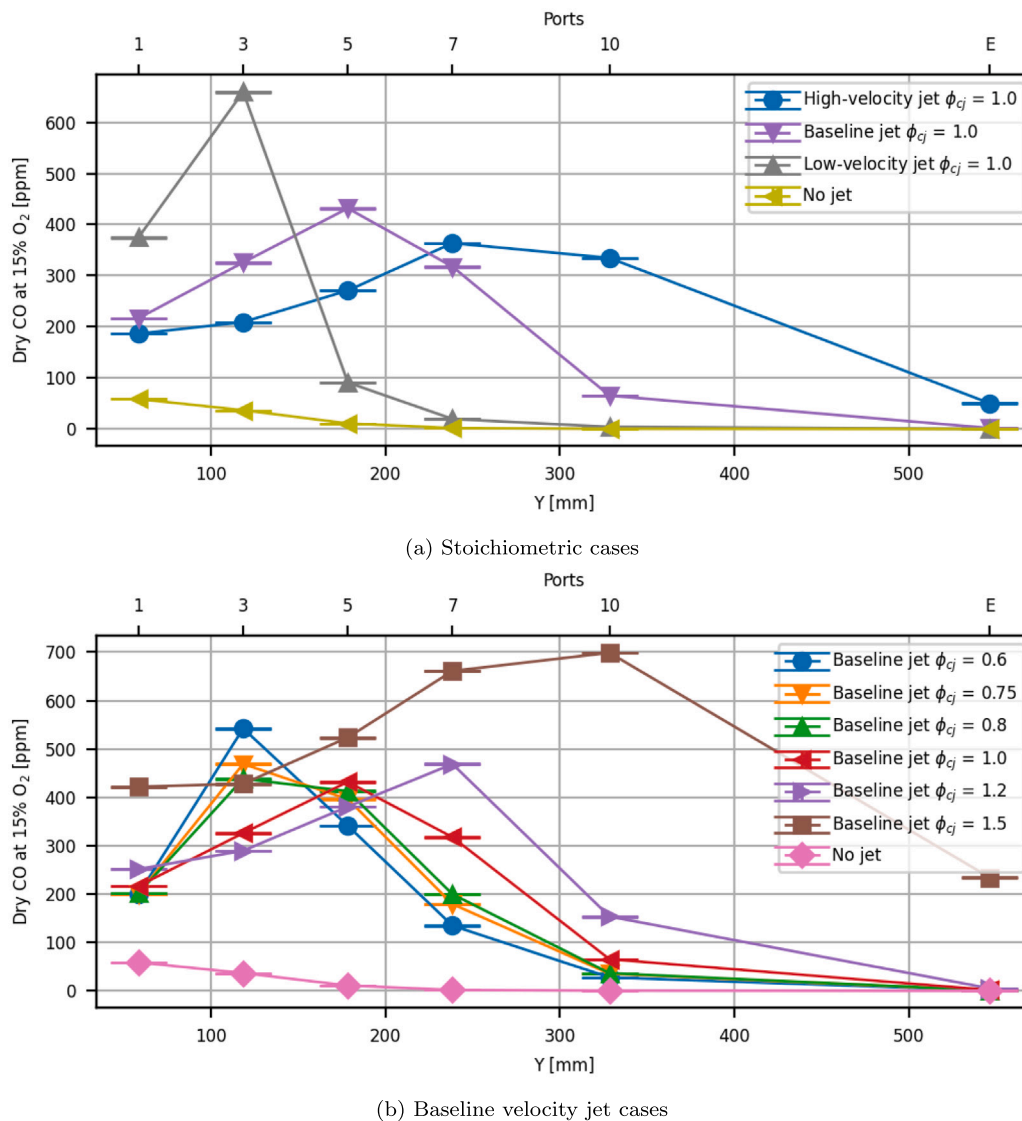


Fig. 15. Streamwise centerline measurements of dry CO at 15% O₂.

3.6. The effect of diluents

The effect of dilution with CO₂ over N₂ is studied by adding these diluents to the coflow mixture. At the same time, the total volume flow rate and O₂ concentration are maintained by altering the power and equivalence ratio of the coflow burners. In Figs. 18(a) and 18(b), the NO and CO are plotted as a function of downstream distance from the jet exit for the stoichiometric baseline velocity jet case and no-jet case with either 20 lpm of N₂ or CO₂ added to the coflow. The previously observed trough in NO is also observed when diluting with nitrogen. However, it is not present when CO₂ is used; the NO concentration keeps dropping until the end of the combustion chamber in that case. A peak in CO can be seen, both when diluting with N₂ and CO₂, but in the CO₂ diluted case, the CO concentration is notably higher also at the inlet and exhaust. This can likely be explained by the decomposition of CO₂ at high temperatures into CO [17,18]. It may also affect the pool of carbon radicals and, thus, extend the region in which NO is being consumed.

Another thing to note is that the point at which the peak in CO is reached is also further downstream when adding diluents compared to the regular stoichiometric baseline jet velocity case; the addition of diluent has also resulted in an elongated combustion zone.

In Fig. 18(c), the CH₄ concentration has been plotted for the cases with added N₂ or CO₂. In the CO₂ diluted case, it can be seen that, just like was observed in the CO plot, there remains a notable concentration of methane in the exhaust gas mixture, while for the N₂ diluted case, the methane concentration at the exhaust is below 10 ppm; in that case, combustion does complete.

It can also be seen that the diluent influences the coflow burners' flames. Dilution with CO₂ results in a higher CO, likely due to the decomposition of CO₂ at high temperatures [17,18], but also results in a decrease in NO as compared to dilution with N₂. The difference in NO could be explained by a reduction in temperature due to the higher thermal capacity per mole of CO₂ as compared to N₂ [24].

4. Summary and conclusion

This paper presents a novel Enclosed Jet-in-Hot-Coflow burner. This new burner overcomes some limitations of earlier open jet-in-hot-coflow setups, which had laboratory air entrainment and lacked system-level exhaust emission measurements, making it challenging to characterize different fuels for emissions under similar operating conditions. Further, the central jet in this new setup injects fuel and oxidizer in a premixed configuration, adding to the diversity of data available for such flames.

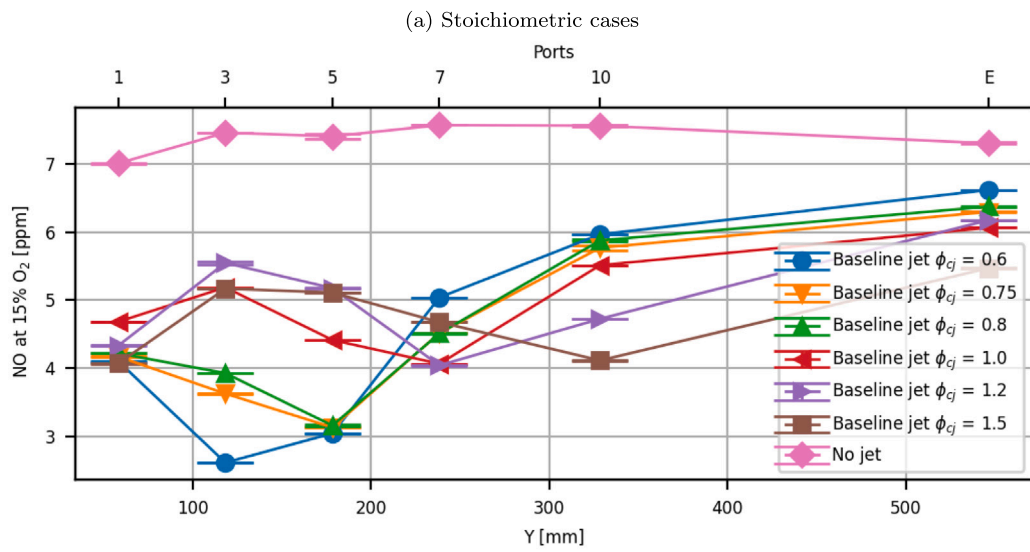
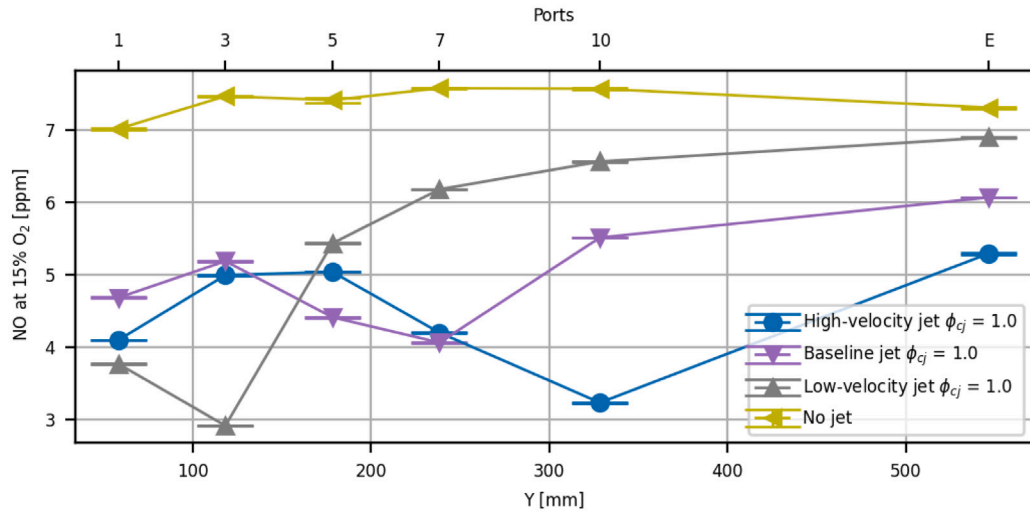


Fig. 16. Streamwise centerline measurements of NO at 15% O₂.

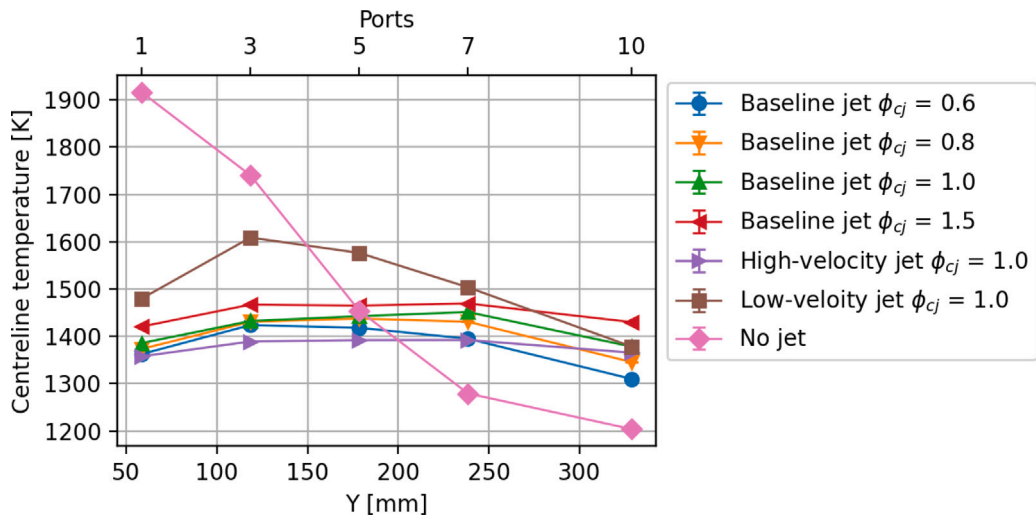


Fig. 17. Streamwise centerline measurements of the temperature in the combustion chamber.

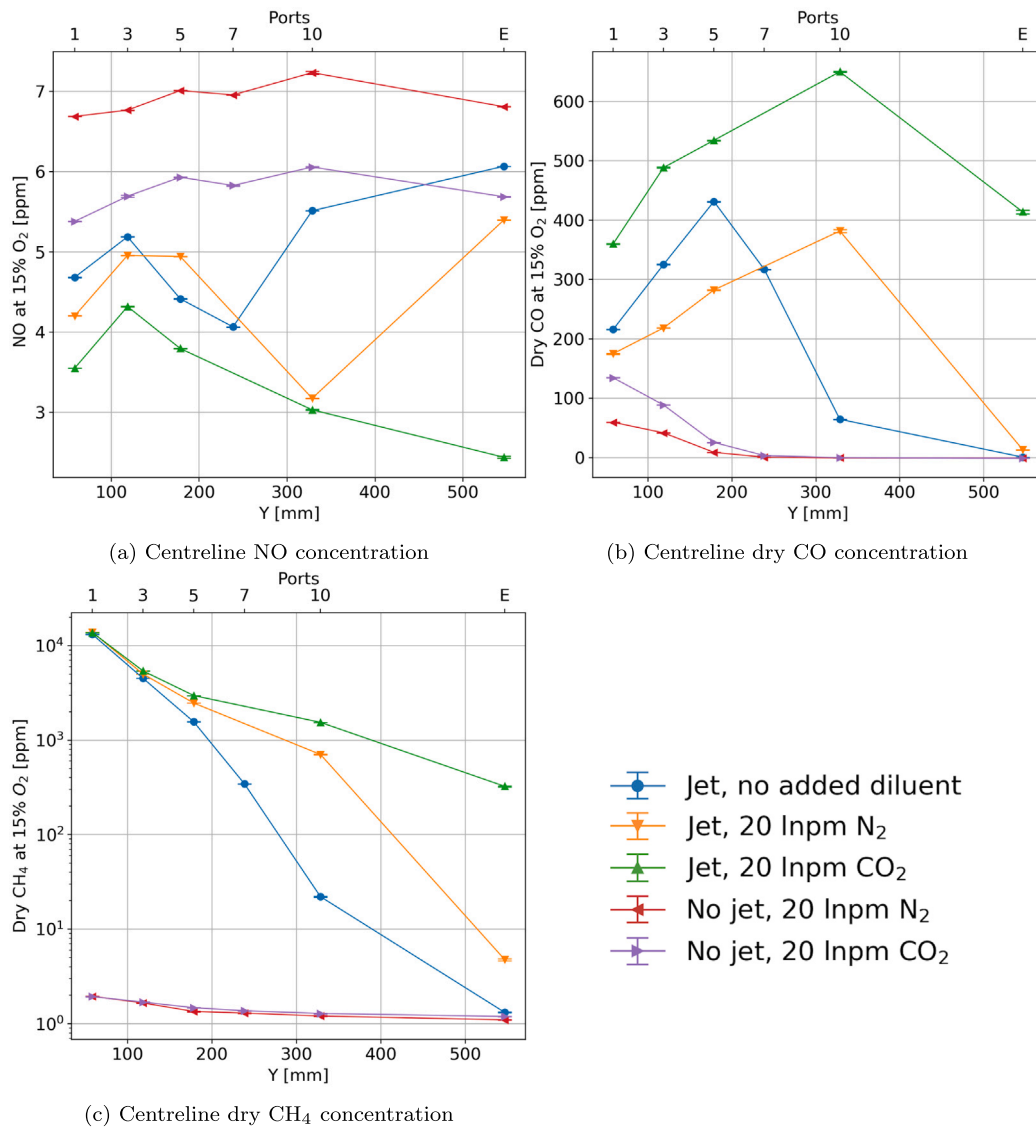


Fig. 18. Baseline jet at $\phi_{c,j} = 1.0$ or no-jet with 20Inpm of CO₂ or N₂ added to the coflow.

The system was operated with CH₄-Air mixture in the jet and the coflow. The coflow was kept constant at 1% O₂, $\phi = 0.95$, thermal power of 11 kW, and bulk velocity of 1.32 m/s. When diluents were added, all parameters were almost constant, except for the power, which was reduced to maintain the same bulk velocity. The central jet velocity was varied such that the system had a global O₂ variation between 1%–5% at the chamber inlet. Further, sensitivity to ϕ was tested by varying ϕ of the central jet.

O₂, CH₄ and CO measurements showed that flameless combustion was achieved in this setup. Furthermore, low flame luminosity and low NO concentrations, which are both characteristic properties of flameless combustion, were also observed in the presented experiments.

The flow field was measured using stereo PIV, the topology of the reaction zone was qualitatively captured using chemiluminescence imaging, and the exhaust emissions from the combustor were measured using a gas analyzer unit. Further, the temperature and species profile along the centerline of the combustor were measured by inserting probes through access ports mounted on a plate installed on one of the sides of the octagonal chamber.

The non-reacting flow field measurements were used to correct the thermocouple measurements, provide reference turbulence data that could be used for numerical model validation in the future, and provide

insights that have been used to understand the transport of species within the chamber.

NO formation in this combustor is sensitive to jet velocity and equivalence ratio, except for the low-velocity jet case, for which the NO_x concentration at the exhaust is almost the same for all equivalence ratios. In the low-velocity jet case, the reaction zone is established upstream. As jet velocity increases, residence time decreases. This creates a situation where the slow NO_x formation process competes with NO_x reburning, which occurs due to the presence of CO, CH₄, and other carbon-based radicals as is well established in literature [9]. Further, increasing ϕ provides a suitable carbon-based radical pool that aids in the NO_x reburning leading to a reduction in NO at the exhaust.

Increasing the central jet velocity and equivalence ratio shifts the reaction zone downstream and enlarges it, as is seen from the chemiluminescence images and CO measurements. A higher jet velocity leads to lower residence time, shifting the reaction zone downstream. A second reason is the change in autoignition delay time with the equivalence ratio. A change in CH₄-air ratio in the central jet leads to a change in the specific heat capacity (C_p) of the mixture. Assuming that ignition kernel formation is initiated by mixing fresh reactants with some hot products from the coflow, a change in reactant mixture C_p would change the final mixture temperature. Increasing ϕ leads to higher C_p , thus, lower

mixture temperature and higher ignition delay time. This causes a downstream shift of the reaction zone and broadening.

Dilution with either N₂ or CO₂ enlarges the combustion zone and decreases NO concentration at the exhaust. The temperature reduction due to the decrease in coflow burner power and the addition of cold diluents is likely a significant factor. Of the two diluents, the addition of CO₂ is found to lower NO but can increase CH₄ and CO levels in the exhaust. In literature, several effects of CO₂ addition on the progression of combustion and formation of NO are discussed, such as the decomposition of CO₂ in CO, which results in a depletion of the hydrogen radical pool [17,18]. However, the effect of the lower temperature inside the combustion chamber, due to the higher thermal capacity of CO₂ per mole, also likely plays a significant role.

Further investigations into this combustion regime can now be undertaken. The location and extent of the combustion zone have been mapped under various operating conditions, enabling subsequent detailed analysis of the regime using high-fidelity laser-based diagnostic techniques. Additionally, the operational regime of the combustor can be further expanded by integrating a coflow burner into the mixing duct, allowing for a greater volume flow rate in the coflow, eliminating the recirculation zone, and attaining higher temperatures inside the combustion chamber.

CRedit authorship contribution statement

Thimo van den Berg: Writing – original draft, Visualization, Methodology, Investigation. **Rishikesh Sampat:** Writing – review & editing, Supervision, Methodology, Formal analysis. **Arvind Gangoli Rao:** Writing – review & editing, Supervision.

Declaration of competing interest

The authors declare that they have no known competing financial interests or personal relationships that could have appeared to influence the work reported in this paper.

Acknowledgment

Rishikesh Sampat would like to acknowledge funding from the PUREJET project, co-sponsored by the Topsector Energie program from the RVO, Dutch Ministry of Economic Affairs.

Data availability

Data will be made available on request.

References

- [1] Maruhashi J, Grewe V, Frömming C, Jöckel P, Dedoussi IC. Transport patterns of global aviation NO_x and their short-term O₃ radiative forcing – a machine learning approach. *Atmos Chem Phys* 2022;22(21):14253–82. <http://dx.doi.org/10.5194/acp-22-14253-2022>.
- [2] USEPA LU - US Environmental Protection Agency. Integrated Science Assessment for Oxides of Nitrogen (Final Report). Washington D.C.: Contract No.: EPA/600/R-08/071; 2016, URL http://ofmpub.epa.gov/eims/eimscmm.getfile?p_download_id=526855.
- [3] Feng S, Gao D, Liao F, Zhou F, Wang X. The health effects of ambient PM_{2.5} and potential mechanisms. *Ecotoxicol Environ Safety* 2016;128:67–74. <http://dx.doi.org/10.1016/j.ecoenv.2016.01.030>.
- [4] Perpignan AA, Gangoli Rao A, Roekaerts DJ. Flameless combustion and its potential towards gas turbines. *Prog Energy Combust Sci* 2018;69:28–62. <http://dx.doi.org/10.1016/j.pecs.2018.06.002>.
- [5] Gangoli Rao A, Levy Y. A new combustion methodology for low emission gas turbine engines. In: 8th HiTACG conference. 2010, p. 1–11.
- [6] Warnatz J, Maas U, Dibble R. *Combustion*. fourth ed.. Springer; 2006.
- [7] Pennell DA, Bothien MR, Ciani A, Granet V, Singla G, Thorpe S, Wickstroem A, Oumejjoud K, Yaquinto M. An introduction to the ansaldo GT36 constant pressure sequential combustor. In: Proceedings of ASME turbo expo 2017: technical conference and exposition. Charlotte; 2017.
- [8] Gangoli Rao A, Yin F, Van Buijtenen JP. A hybrid engine concept for multi-fuel blended wing body. *Aircr Eng Aerosp Technol* 2014;86(6):483–93. <http://dx.doi.org/10.1108/AEAT-04-2014-0054>.
- [9] Glarborg P, Miller JA, Ruscic B, Klippenstein SJ. Modeling nitrogen chemistry in combustion. 2018, p. 31–68. <http://dx.doi.org/10.1016/j.pecs.2018.01.002>.
- [10] Wünnig JA, Wünnig JG. Flameless oxidation to reduce thermal NO-formation. *Prog Energy Combust Sci* 1997;23(1):81–94. [http://dx.doi.org/10.1016/s0360-1285\(97\)00006-3](http://dx.doi.org/10.1016/s0360-1285(97)00006-3).
- [11] Cavaliere A, De Joannon M. Mild combustion. *Prog Energy Combust Sci* 2004;30(4):329–66. <http://dx.doi.org/10.1016/j.pecs.2004.02.003>.
- [12] Oberlack M, Arlitt R, Peters N. On stochastic Damköhler number variations in a homogeneous flow reactor. *Combust Theory Model* 2000;4:495–509. <http://dx.doi.org/10.1088/1364-7830/4/4/307>.
- [13] Evans MJ, Medwell PR, Wu H, Stagni A, Ihme M. Classification and lift-off height prediction of non-premixed MILD and autoignitive flames. *Proc. Combust. Inst.* 2017;36(3):4297–304. <http://dx.doi.org/10.1016/j.proci.2016.06.013>.
- [14] Dally BB, Karpets AN, Barlow RS. Structure of turbulent non-premixed jet flames in a diluted hot coflow. *Proc. Combust. Inst.* 2002;29(1):1147–54. [http://dx.doi.org/10.1016/S1540-7489\(02\)80145-6](http://dx.doi.org/10.1016/S1540-7489(02)80145-6).
- [15] Oldenhof E, Tummers MJ, van Veen EH, Roekaerts DJ. Role of entrainment in the stabilisation of jet-in-hot-coflow flames. *Combust Flame* 2011;158(8):1553–63. <http://dx.doi.org/10.1016/j.combustflame.2010.12.018>.
- [16] Sadanandan R, Lückerrath R, Meier W, Wahl C. Flame characteristics and emissions in flameless combustion under gas turbine relevant conditions. *J Propuls Power* 2011;27(5):970–80. <http://dx.doi.org/10.2514/1.50302>.
- [17] Park J, Kim SG, Lee KM, Kim TK. Chemical effect of diluents on flame structure and NO emission characteristic in methane-air counterflow diffusion flame. *Int J Energy Res* 2002;26(13):1141–60. <http://dx.doi.org/10.1002/er.841>.
- [18] Westbrook CK, Dryer FL. Chemical kinetic modeling of hydrocarbon combustion. *Prog Energy Combust Sci* 1984;10(1):1–57. [http://dx.doi.org/10.1016/0360-1285\(84\)90118-7](http://dx.doi.org/10.1016/0360-1285(84)90118-7).
- [19] Sabia P, Lubrano Lavadera M, Giudicianni P, Sorrentino G, Ragucci R, de Joannon M, Lubrano M, Giudicianni P, Sorrentino G, Ragucci R. CO₂ and H₂O effect on propane auto-ignition delay times under mild combustion operative conditions. *Combust Flame* 2015;162(3):533–43. <http://dx.doi.org/10.1016/j.combustflame.2014.08.009>.
- [20] Benedict LH, Gould RD. Towards better uncertainty estimates for turbulence statistics. *Exp Fluids* 1996;22:129–36.
- [21] Jiménez S. Relevance of heat conduction in the correction and interpretation of high temperature, fine wire thermocouple measurements. *Combust Flame* 2022;240. <http://dx.doi.org/10.1016/j.combustflame.2022.112022>.
- [22] Shaddix C. Correcting thermocouple measurements for radiation loss: A critical review. 1999.
- [23] Harnby N, Edwards MF, Nienow AW. *Mixing in the Process Industries*. second ed.. Butterworth-Heinemann; 1985.
- [24] Chase Jr M. NIST-JANAF thermochemical tables. 1998, p. 1–1951.